

# PROCEEDINGS OF SPIE

[SPIDigitalLibrary.org/conference-proceedings-of-spie](https://www.spiedigitallibrary.org/conference-proceedings-of-spie)

## Internally coupled piezoelectric metamaterial beam with multi-functionalities

Guobiao Hu, Lihua Tang, Raj Das, Kean Aw

Guobiao Hu, Lihua Tang, Raj Das, Kean Aw, "Internally coupled piezoelectric metamaterial beam with multi-functionalities," Proc. SPIE 10595, Active and Passive Smart Structures and Integrated Systems XII, 1059516 (19 March 2018); doi: 10.1117/12.2296451

**SPIE.**

Event: SPIE Smart Structures and Materials + Nondestructive Evaluation and Health Monitoring, 2018, Denver, Colorado, United States

# Internally Coupled Piezoelectric Metamaterial Beam with Multifunctionalities

Guobiao HU<sup>a</sup>, Lihua TANG<sup>a\*</sup>, Raj DAS<sup>b</sup>, Kean AW<sup>a</sup>

<sup>a</sup>Department of Mechanical Engineering, University of Auckland, 20 Symonds Street, Auckland 1010, New Zealand; <sup>b</sup>School of Engineering, RMIT University, GPO Box 2476, Melbourne, VIC 3001, Australia

## ABSTRACT

A piezoelectric metamaterial beam is proposed in this paper for both vibration suppression and energy harvesting. Additional springs are introduced to create internal coupling alternately between local resonators. Each resonator is associated with a piezoelectric element for producing electrical energy. First, the mathematical model of the piezoelectric metamaterial beam is developed. The analytical solutions of the transmittance of the system and the open-circuit voltage responses of the piezoelectric elements are derived. As compared to the conventional counterpart without internal coupling, it is found that the energy harvesting performance is significantly reinforced in the low frequency range and the vibration suppression performance is slightly enhanced due to the appearance of an additional band gap. Subsequently, an equivalent finite element model – model A for verifying analytical solutions is developed. The lumped local resonators in the analytical model are modelled by using cantilevers with tip masses in the finite element model. The tip masses are alternately coupled with one-dimensional two-node spring elements. The finite element analysis results show good agreement with the analytical results for both the transmittance of the system and the open-circuit voltage responses of the piezoelectric elements. Finally, a model B with a more practical realization of the internal coupling is established. The coupling spring is replaced by a beam connection. The finite element analysis results show that the behavior of model B is different from model A and is not equivalent to the proposed analytical model. No significant enhancement in terms of energy harvesting is observed but a remarkably enhanced vibration suppression performance appears in model B. The difference between the two models is then discussed.

**Keywords:** Piezoelectric, energy harvesting, metamaterial, vibration suppression

## 1. INTRODUCTION

Elastic metamaterials (EMMs) with artificially engineered microstructures possess several unique properties including negative refraction [1, 2], negative modulus [3, 4], negative effective density [5, 6], to name a few. Researchers have been attracted to explore the applications of EMMs for various kinds of applications [7-11], one of which is low frequency vibration suppression [12-15]. The ability of EMMs for vibration suppression arises from their band gap phenomenon due to the out-of-phase motion of the introduced microstructures (local resonators) when vibrations occur near resonance [16, 17]. In recent years, the applications of metamaterials have been extended into the field of vibration energy harvesting [18-20]. Shen et al. [10] designed a metamaterial plate consisting of an array of spiral beams as conversion medium for energy harvesting and claimed that the output power was enhanced at multiple resonant frequencies in a low frequency range. Mikoshiba *et al.* [21] proposed an energy harvesting system with a periodic structure embedded with multiple local resonators made of spring-suspended magnets. Hu *et al.* [22] proposed a tunable metamaterial with embedded piezoelectric elements for achieving simultaneous energy harvesting and vibration suppression. A more recent study [23] extended their work to a piezoelectric metamaterial beam through distributed parameter modelling. They investigated this piezoelectric metamaterial beam from both the vibration suppression and energy harvesting perspectives. A recent review paper on the topic of metamaterial-inspired energy harvesting can be referred to [24].

On the basis of the models presented in [25] and [23], this paper proposes an internally coupled metamaterial beam embedded with piezoelectric elements. Such a beam based on a distributed parameter model represents a more practical structure of internally coupled metamaterials. The phenomenon of the appearance of the additional band gap due to the

---

\* l.tang@auckland.ac.nz, phone: +64 9 373 7599 ext 89535

internal coupling discovered in [25] is still observed in the distributed parameter model. As the vibration suppression performance of metamaterials is determined by band gaps, the occurrence of the additional band gap can enhance the vibration suppression ability. In addition, the idea of piezoelectric metamaterial beam introduced in [31] for energy harvesting is extended in this proposed model and an improved performance is achieved. First, based on the Euler-Bernoulli beam theory, the finitely long model of the proposed modified metamaterial beam is developed and its transmittance is calculated. Bands gaps of the modified metamaterial is observed and identified from the transmittance. Subsequently, under weak coupling conditions, by embedding piezoelectric elements with local resonators, the energy harvesting performance of the system is analytically investigated. In addition to the analytical study, two types of finite element (FE) models (termed models A and B) are established. In model A, each lumped local resonator in the analytical model is modelled by using a pair of cantilever beams with tip masses. The tip masses are alternately coupled with ideal springs. In model B, the ideal spring connection is replaced by a beam connection, which is analogous to a more practical implementation. Both vibration suppression and energy harvesting performances of these two models are analysed and compared. The difference between the two models is discussed.

## 2. ANALYTICAL MODELLING

### 2.1 Vibration suppression of modified metamaterial beam

This section describes the structure of the modified metamaterial beam as shown in Figure 1 and investigates its vibration suppression performance through the transmittance of a finitely long model. The host plain beam is of length  $L$ . There are  $2S$  resonators with mass  $m$ , damping  $c$  and spring  $k$  periodically placed onto the host beam at a uniform distance of  $d$ . The left-hand side of the beam is clamped on a base that experiences a harmonic excitation  $w_b(t) = W_b e^{i\omega t}$ . The base excitation is controlled at a constant acceleration  $a_{cc} = -\omega^2 W_b$ . By adopting the Euler-Bernoulli beam theory, the governing equation of the metamaterial beam is written as:

$$EI \frac{\partial^4 w_{rel}(x,t)}{\partial x^4} + c_s I \frac{\partial^5 w_{rel}(x,t)}{\partial x^4 \partial t} + \rho A_{cs} \frac{\partial^2 w_{rel}(x,t)}{\partial t^2} = \rho A_{cs} a_{cc} e^{i\omega t} - \sum_{j=1}^S [F_j^l \delta(x-x_j^l) + F_j^r \delta(x-x_j^r)] e^{i\omega t} \quad (1)$$

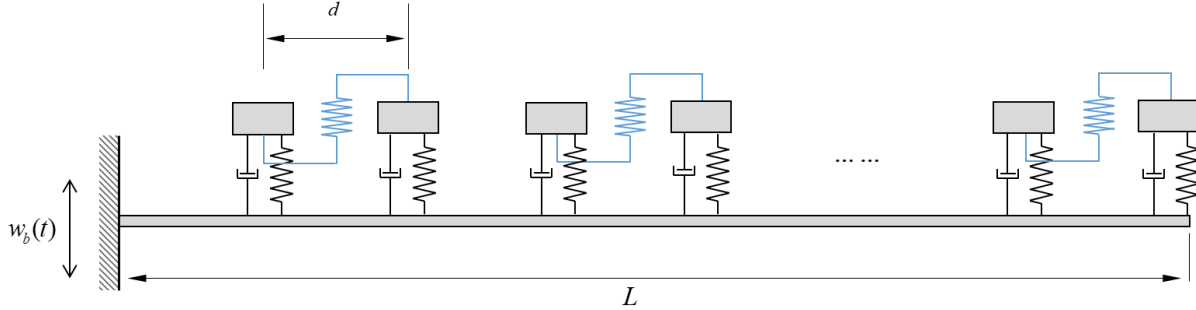


Figure 1. Finitely long model of the internally coupled metamaterial beam.

where  $EI$ ,  $\rho$ ,  $A_{cs}$  are the bending stiffness, density and cross-section area of the beam, respectively;  $w_{rel}(x,t)$  is the relative transverse displacement between the beam  $w(x,t)$  and the base  $w_b(t)$ ;  $c_s$  is the equivalent strain rate damping coefficient;  $F_j^l$  and  $F_j^r$  are the reaction forces exerted by the left and right resonators in the  $j^{\text{th}}$  cell onto the beam during vibration, respectively;  $\delta(x)$  is the Dirac delta function. The equations of motion for resonators are:

$$\begin{cases} m\ddot{u}_j^l(t) + c\dot{u}_j^l(t) + ku_j^l(t) + k_c(u_j^l(t) + w(x_j^l, t) - u_j^r(t) - w(x_j^r, t)) = -m\ddot{w}(x_j^l, t) \\ m\ddot{u}_j^r(t) + c\dot{u}_j^r(t) + ku_j^r(t) + k_c(u_j^r(t) + w(x_j^r, t) - u_j^l(t) - w(x_j^l, t)) = -m\ddot{w}(x_j^r, t) \end{cases} \quad (2)$$

where  $u_j^l(t)$  and  $u_j^r(t)$  are the displacements of the left and right resonator masses in the  $j^{\text{th}}$  cell relative to the host beam, respectively, and they are coupled by spring  $k_c$ . Using the modal superposition method, the relative displacement along the beam can be written as:

$$w_{rel}(x, t) = \sum_{k=1}^{\infty} \phi_k(x) \eta_k(t) \quad (k = 1, 2, 3 \dots) \quad (3)$$

where  $\phi_k(x)$  are the normalized mode shape functions of the plain beam without resonators and  $\eta_k(t)$  are the modal coordinates. Substituting Eq.(3) into (1), multiplying by  $\phi_n(x)$  and integrating over the beam length from 0 to  $L$ , then using the orthogonal conditions ( $\int_0^L \rho A_{cs} \phi_k(x) \phi_n(x) dx = \delta_{nk}$ ,  $\int_0^L EI \frac{d^4 \phi_k(x)}{dx^4} \phi_n(x) dx = \omega_n^2 \delta_{nk}$ ), the modal governing equation is obtained as:

$$\ddot{\eta}_n(t) + 2\zeta_n \omega_n \dot{\eta}_n(t) + \omega_n^2 \eta_n(t) = \rho A_{cs} a_{cc} e^{i\omega t} \int_0^L \phi_n(x) dx - \sum_{j=1}^S \left[ F_j^l \phi_n(x_j^l) e^{i\omega t} + F_j^r \phi_n(x_j^r) e^{i\omega t} \right] \quad (4)$$

where  $\zeta_n = \frac{c_s I \omega_n}{2E}$ . The expression of  $\eta_n(t)$  can be obtained from Eq.(4). Substituting the derived  $\eta_n(t)$  into Eq.(3) yields the solution of the relative displacement in a closed-form as:

$$w_{rel}(x, t) = \sum_{k=1}^{\infty} \phi_k(x) \frac{\rho A_{cs} a_{cc} \int_0^L \phi_k(x) dx - \sum_{j=1}^S \left[ F_j^l \phi_k(x_j^l) + F_j^r \phi_k(x_j^r) \right]}{\omega_k^2 - \omega^2 + 2i\zeta_k \omega_k \omega} e^{i\omega t} \quad (5)$$

From Eq.(2), one obtains:

$$\begin{cases} u_j^l(t) = \alpha_1 w_{rel}(x_j^l, t) + \alpha_2 w_{rel}(x_j^r, t) + \alpha_3 w_b(t) \\ u_j^r(t) = \alpha_2 w_{rel}(x_j^l, t) + \alpha_1 w_{rel}(x_j^r, t) + \alpha_3 w_b(t) \end{cases} \quad (6)$$

where

$$\begin{cases} \alpha_1 = \frac{[k_c^2 - (k_c - m\omega^2)(k + k_c - m\omega^2 + i\omega c)]}{(k + k_c - m\omega^2 + i\omega c)^2 - k_c^2} \\ \alpha_2 = \frac{k_c(k + i\omega c)}{(k + k_c - m\omega^2 + i\omega c)^2 - k_c^2} \\ \alpha_3 = \frac{[k_c^2 - (k_c - m\omega^2)(k + k_c - m\omega^2 + i\omega c)] + k_c(k + i\omega c)}{(k + k_c - m\omega^2 + i\omega c)^2 - k_c^2} \end{cases}$$

The reaction forces exerted by the left and right resonators in the  $j^{\text{th}}$  cell onto the beam are expressed as:

$$\begin{cases} f_j^l = -[c\dot{u}_j^l(t) + k u_j^l(t)] = -(k + i\omega c) \alpha_1 w_{rel}(x_j^l, t) + \alpha_2 w_{rel}(x_j^r, t) + \alpha_3 w_b(t) \\ f_j^r = -[c\dot{u}_j^r(t) + k u_j^r(t)] = -(k + i\omega c) \alpha_2 w_{rel}(x_j^l, t) + \alpha_1 w_{rel}(x_j^r, t) + \alpha_3 w_b(t) \end{cases} \quad (7)$$

Substituting Eq.(5) into Eq.(7) gives the expressions of the force amplitudes as:

$$\left\{ \begin{array}{l} F_j^l = -(k + i\omega c) \left\{ \begin{array}{l} \alpha_1 \times \sum_{k=1}^{\infty} \phi_k(x_j^l) \frac{\rho A_{cs} a_{cc} \int_0^L \phi_k(x) dx - \sum_{h=1}^S [F_h^l \phi_k(x_h^l) + F_h^r \phi_k(x_h^r)]}{\omega_k^2 - \omega^2 + 2i\zeta_k \omega_k \omega} \\ + \alpha_2 \times \sum_{k=1}^{\infty} \phi_k(x_j^r) \frac{\rho A_{cs} a_{cc} \int_0^L \phi_k(x) dx - \sum_{h=1}^S [F_h^l \phi_k(x_h^l) + F_h^r \phi_k(x_h^r)]}{\omega_k^2 - \omega^2 + 2i\zeta_k \omega_k \omega} + \alpha_3 \frac{a_{cc}}{\omega^2} \end{array} \right\} \\ F_j^r = -(k + i\omega c) \left\{ \begin{array}{l} \alpha_2 \times \sum_{k=1}^{\infty} \phi_k(x_j^l) \frac{\rho A_{cs} a_{cc} \int_0^L \phi_k(x) dx - \sum_{h=1}^S [F_h^l \phi_k(x_h^l) + F_h^r \phi_k(x_h^r)]}{\omega_k^2 - \omega^2 + 2i\zeta_k \omega_k \omega} \\ + \alpha_1 \times \sum_{k=1}^{\infty} \phi_k(x_j^r) \frac{\rho A_{cs} a_{cc} \int_0^L \phi_k(x) dx - \sum_{h=1}^S [F_h^l \phi_k(x_h^l) + F_h^r \phi_k(x_h^r)]}{\omega_k^2 - \omega^2 + 2i\zeta_k \omega_k \omega} + \alpha_3 \frac{a_{cc}}{\omega^2} \end{array} \right\} \end{array} \right. \quad (8)$$

Rearrange the 2S reaction force equations, i.e.,  $F_1^l, F_2^l, \dots, F_S^l, F_1^r, F_2^r, \dots, F_S^r$  as follows:

$$\left\{ \begin{array}{l} a_{1,1} F_1^l + a_{1,2} F_2^l + \dots + a_{1,S} F_S^l + a_{1,S+1} F_1^r + a_{1,S+2} F_2^r + \dots + a_{1,2S} F_S^r = b_1 \\ \dots \\ a_{j,1} F_1^l + a_{j,2} F_2^l + \dots + a_{j,S} F_S^l + a_{j,S+1} F_1^r + a_{j,S+2} F_2^r + \dots + a_{j,2S} F_S^r = b_j \\ \dots \\ a_{S,1} F_1^l + a_{S,2} F_2^l + \dots + a_{S,S} F_S^l + a_{S,S+1} F_1^r + a_{S,S+2} F_2^r + \dots + a_{S,2S} F_S^r = b_S \\ a_{S+1,1} F_1^l + a_{S+1,2} F_2^l + \dots + a_{S+1,S} F_S^l + a_{S+1,S+1} F_1^r + a_{S+1,S+2} F_2^r + \dots + a_{S+1,2S} F_S^r = b_{S+1} \\ \dots \\ a_{S+j,1} F_1^l + a_{S+j,2} F_2^l + \dots + a_{S+j,S} F_S^l + a_{S+j,S+1} F_1^r + a_{S+j,S+2} F_2^r + \dots + a_{S+j,2S} F_S^r = b_{S+j} \\ \dots \\ a_{2S,1} F_1^l + a_{2S,2} F_2^l + \dots + a_{2S,S} F_S^l + a_{2S,S+1} F_1^r + a_{2S,S+2} F_2^r + \dots + a_{2S,2S} F_S^r = b_{2S} \end{array} \right. \quad (9)$$

where,

$$a_{j,h} = \left\{ \begin{array}{l} \left( \alpha_1 \times \sum_{k=1}^{\infty} \frac{\phi_k(x_j^l) \phi_k(x_h^l)}{\omega_k^2 - \omega^2 + 2i\zeta_k \omega_k \omega} + \alpha_2 \times \sum_{k=1}^{\infty} \frac{\phi_k(x_j^r) \phi_k(x_h^l)}{\omega_k^2 - \omega^2 + 2i\zeta_k \omega_k \omega} \right) \text{ for } 1 \leq j \leq S; 1 \leq h \leq S \\ \left( \alpha_1 \times \sum_{k=1}^{\infty} \frac{\phi_k(x_j^l) \phi_k(x_{(h-S)}^r)}{\omega_k^2 - \omega^2 + 2i\zeta_k \omega_k \omega} + \alpha_2 \times \sum_{k=1}^{\infty} \frac{\phi_k(x_j^r) \phi_k(x_{(h-S)}^r)}{\omega_k^2 - \omega^2 + 2i\zeta_k \omega_k \omega} \right) \text{ for } 1 \leq j \leq S; S+1 \leq h \leq 2S \\ \left( \alpha_2 \times \sum_{k=1}^{\infty} \frac{\phi_k(x_{(j-S)}^l) \phi_k(x_h^l)}{\omega_k^2 - \omega^2 + 2i\zeta_k \omega_k \omega} + \alpha_1 \times \sum_{k=1}^{\infty} \frac{\phi_k(x_{(j-S)}^r) \phi_k(x_h^l)}{\omega_k^2 - \omega^2 + 2i\zeta_k \omega_k \omega} \right) \text{ for } S+1 \leq j \leq 2S; 1 \leq h \leq S \\ \left( \alpha_2 \times \sum_{k=1}^{\infty} \frac{\phi_k(x_{(j-S)}^l) \phi_k(x_{(h-S)}^r)}{\omega_k^2 - \omega^2 + 2i\zeta_k \omega_k \omega} + \alpha_1 \times \sum_{k=1}^{\infty} \frac{\phi_k(x_{(j-S)}^r) \phi_k(x_{(h-S)}^r)}{\omega_k^2 - \omega^2 + 2i\zeta_k \omega_k \omega} \right) \text{ for } S+1 \leq j \leq 2S; S+1 \leq h \leq 2S \end{array} \right.$$

$$a_{j,j} = \begin{cases} \left( \alpha_1 \times \sum_{k=1}^{\infty} \frac{\phi_k(x_j^l) \phi_k(x_j^r)}{\omega_k^2 - \omega^2 + 2i\zeta_k \omega_k \omega} + \alpha_2 \times \sum_{k=1}^{\infty} \frac{\phi_k(x_j^r) \phi_k(x_j^l)}{\omega_k^2 - \omega^2 + 2i\zeta_k \omega_k \omega} - \frac{1}{(k + i\omega c)} \right) & \text{for } 1 \leq j \leq S \\ \left( \alpha_2 \times \sum_{k=1}^{\infty} \frac{\phi_k(x_{(j-S)}^l) \phi_k(x_{(j-S)}^r)}{\omega_k^2 - \omega^2 + 2i\zeta_k \omega_k \omega} + \alpha_1 \times \sum_{k=1}^{\infty} \frac{\phi_k(x_{(j-S)}^r) \phi_k(x_{(j-S)}^l)}{\omega_k^2 - \omega^2 + 2i\zeta_k \omega_k \omega} - \frac{1}{(k + i\omega c)} \right) & \text{for } S+1 \leq j \leq 2S \end{cases}$$

$$b_j = \begin{cases} \left( \alpha_1 \times \sum_{k=1}^{\infty} \phi_k(x_j^l) \frac{\rho A_{cs} a_{cc} \int_0^L \phi_k(x) dx}{\omega_k^2 - \omega^2 + 2i\zeta_k \omega_k \omega} + \alpha_2 \times \sum_{k=1}^{\infty} \phi_k(x_j^r) \frac{\rho A_{cs} a_{cc} \int_0^L \phi_k(x) dx}{\omega_k^2 - \omega^2 + 2i\zeta_k \omega_k \omega} + \alpha_3 \frac{a_{cc}}{\omega^2} \right) & \text{for } 1 \leq j \leq S \\ \left( \alpha_2 \times \sum_{k=1}^{\infty} \phi_k(x_{(j-S)}^l) \frac{\rho A_{cs} a_{cc} \int_0^L \phi_k(x) dx}{\omega_k^2 - \omega^2 + 2i\zeta_k \omega_k \omega} + \alpha_1 \times \sum_{k=1}^{\infty} \phi_k(x_{(j-S)}^r) \frac{\rho A_{cs} a_{cc} \int_0^L \phi_k(x) dx}{\omega_k^2 - \omega^2 + 2i\zeta_k \omega_k \omega} + \alpha_3 \frac{a_{cc}}{\omega^2} \right) & \text{for } S+1 \leq j \leq 2S \end{cases}$$

From Eq.(9) the  $2S$  values of  $F_j^l$  and  $F_j^r$  can be solved. Substituting them back into Eq.(5) gives the solution of the relative deflection amplitude  $W_{rel}(x)$ . The transmittance of the system is defined and calculated as:

$$\tau = \frac{|W_{rel}(L) + W_b|}{|W_b|} \quad (10)$$

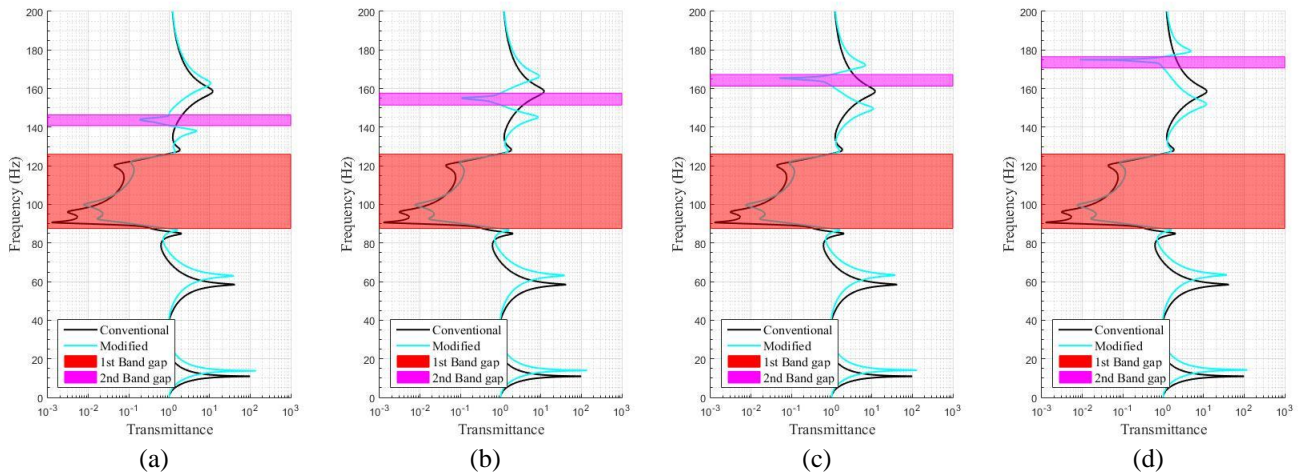


Figure 2. Transmittance of the internally coupled metamaterial beam: (a)  $k_c=0.8k$ ; (b)  $k_c=1.0k$ ; (c)  $k_c=1.2k$ ; (d)  $k_c=1.4k$ .

With the parameters listed in Table 1, for different values of the coupling spring stiffness, the transmittances of the modified metamaterial beam are calculated as shown in Figure 2. It is noteworthy that the model is now assumed to be finitely long. The supplementary information used in the calculation include: material damping ratio 0.009; resonator damping ratio 0.009; beam length 0.45 m (thus incorporating 6 local resonators attached onto the host beam). It can be noted that in the modified metamaterial beam, two band gaps appear due to the existence of the internal coupling. From Figure 2.(a)-(d), for the modified metamaterial beam with given four different coupling springs, the first band gap ranges are (87.6-125.9 Hz), (87.6-126.0 Hz), (87.6-126.1 Hz), and (87.6-126.1 Hz), respectively. The second band gap ranges are (140.9- 146.3 Hz), (151.5-157.6 Hz), (161.4-167.3 Hz), and (170.7-176.5 Hz), respectively. It is found that with the increase of the coupling spring stiffness  $k_c$ , the first band gap is unaffected and almost the same as that of the conventional one (85.9-126.2 Hz). The location of the second band gap moves toward a higher frequency and the width of the second band gap varies. However, since the second band gap is very narrow as compared to the first band gap, its variation is not noticeable.

Table 1. System parameters under investigation.

Parameters	Values
Beam cross-section area $A_{cs}$	$0.020 \times 0.004 \text{ m}^2$
Beam mass density $\rho$	7860 m
Young's Modulus $E$	$200 \times 10^9 \text{ Pa}$
Periodic constant $d$	0.075 m
Local resonator mass $m$	0.0396 kg
Local resonator stiffness $k$	$1.2663 \times 10^4 \text{ N/m}$

## 2.2 Energy harvesting of modified metamaterial beam

A metamaterial based energy harvester with piezoelectric elements was proposed by [22] which was modelled with lumped parameters. This concept was then extended by using distributed parameter modelling which yielded a metamaterial beam [23]. In this paper, by integrating piezoelectric elements, a modified metamaterial beam based piezoelectric energy harvester (PEH) is proposed. The energy harvesting performance is then analytically studied and compared with that of the conventional metamaterial beam PEH presented in [23]. The following study is conducted under the assumption of weak electromechanical coupling conditions. The governing equation of the circuit part is:

$$\frac{v}{R} + C^S \dot{v} - \theta \ddot{u} = 0 \quad (11)$$

where  $\theta$  is the electromechanical coupling coefficient;  $C^S$  is the clamped capacitance of the piezoelectric element;  $R$  is the resistance of the electric resistor shunted to the piezoelectric element;  $v$  is the voltage across the electric resistor  $R$ ;  $u$  is the displacement of the local resonator mass relative to the host beam. Applying Laplace transform, the voltage amplitude is represented by using the amplitude of  $u$ :

$$|V| = \left| \frac{i\theta\omega U}{\frac{1}{R} + i\omega C^S} \right| \quad (12)$$

By finding the limit of  $|V|$  as  $R$  approaches positive infinity, the open-circuit voltage amplitude can be expressed as:

$$|V_{oc}| = \left| \frac{\theta U}{C^S} \right| \quad (13)$$

It can be seen that the open-circuit voltage amplitude is linearly proportional to the relative displacement amplitude  $U$  of the local resonator mass, i.e.,  $|V_{oc}| \propto |U|$ . In the following study for investigating energy harvesting performance, the same system (i.e., with parameters listed in Table 1) whose transmittance was previously studied is re-used. The internal coupling spring stiffness is  $k_c = 13824 \text{ N/m}$ . The electromechanical coupling coefficient  $\theta$  and the clamped capacitance  $C^S$  are  $1.45 \times 10^{-3} \text{ N/V}$  and  $18 \text{ nF}$ , respectively. In addition, for the fairness of comparison and evaluation, the same piezoelectric elements are used in both the conventional and modified metamaterial beam PEHs.

The base excitation is controlled at a constant acceleration  $a_{cc} = -1 \text{ m/s}^2$ . Figure 3.(a) and (b) show the open circuit voltage responses of the piezoelectric elements in the conventional and the modified metamaterial beams, respectively. It is noted that the amplitude of the first peak in  $|V_{oc}|$  response of the modified metamaterial beam is larger than that of the conventional one for about an order of magnitude. Figure 3.(c) and (d) show the first peak responses in Figure 3.(a) and (b) with a higher frequency resolution. In the conventional metamaterial beam, the piezoelectric element attached to the 6<sup>th</sup> local resonator (at the tip of the metamaterial beam) exhibits the largest  $|V_{oc}|$  equal to 30.7 V at 10.95 Hz. This can be explained by the mechanism of the dynamic amplifier [26]. To those local resonators, the host beam serves as a dynamic amplifier. The tip of the host beam undergoes the most violent motion; thus the local resonator at the utmost tip of the beam gains the largest dynamic amplification. However, after introducing the internal coupling, the system behavior changes. The 5<sup>th</sup> local resonator experiences the most significant dynamic amplification at 14.06 Hz and provides a maximum  $|V_{oc}|$  equal to 137.6 V. It can be quantitatively estimated that the maximum  $|V_{oc}|$  of the modified metamaterial beam PEH is about 4.5 times that of the conventional one. Therefore, in terms of energy harvesting, the introduction of the internal coupling can significantly enhance the energy harvesting performance.

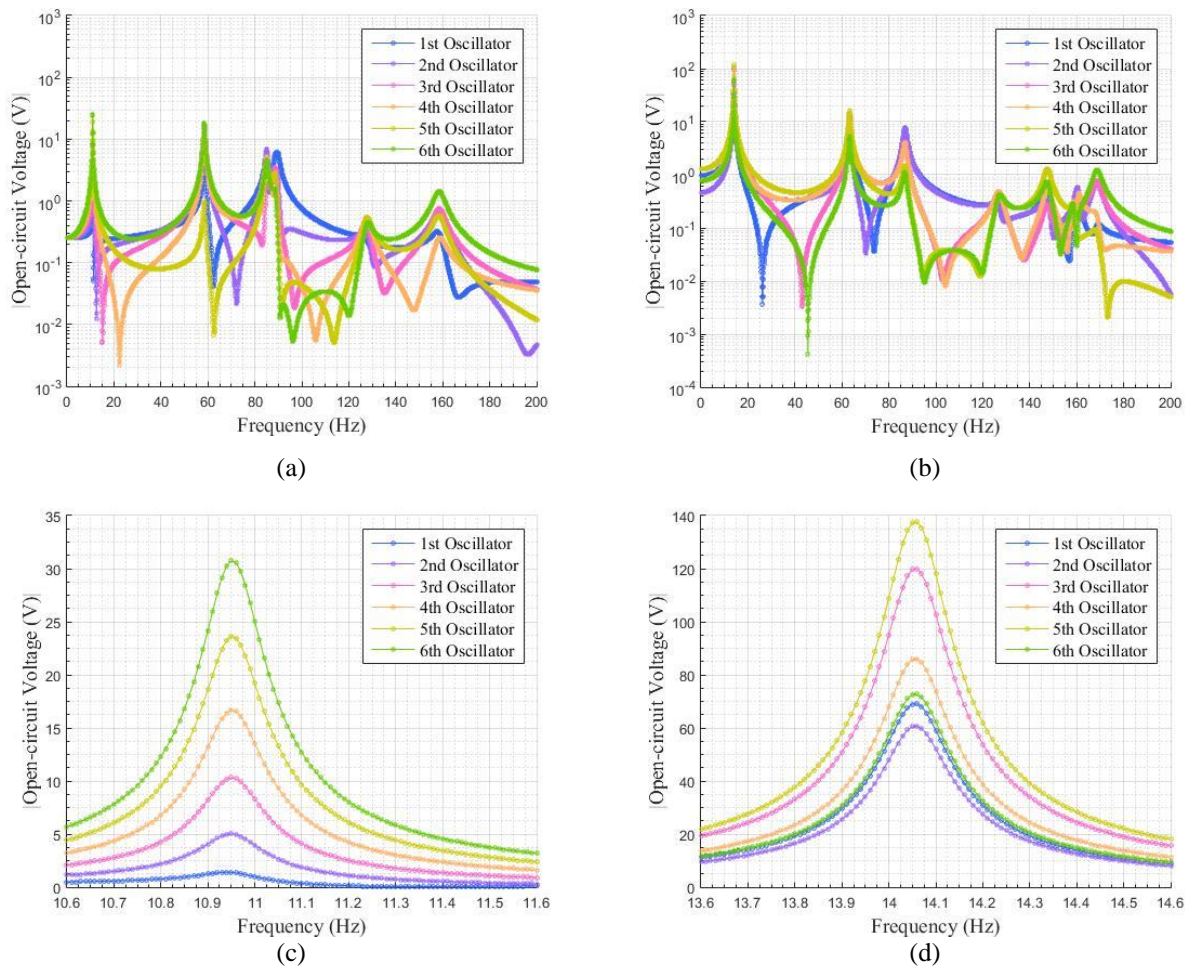


Figure 3. Open circuit voltage responses of piezoelectric elements in: (a) the conventional metamaterial beam and (b) the internally coupled metamaterial beam; Open circuit voltage responses around first resonance with a higher resolution: (c) the conventional metamaterial beam and (d) the internally coupled metamaterial beam.

### 3. FINITE ELEMENT MODELLING

#### 3.1 Modified piezoelectric metamaterial beam - model A

In this section, a finite element model, termed model A (Figure 4.(a)), which is expected to be equivalent to the analytical model, is developed by using the commercial software ANSYS to validate the theoretical studies presented in section 2. In model A, each lumped local resonator was modelled by a pair of cantilevers with tip masses because the dynamic behavior around the fundamental resonance of a cantilever beam with a tip mass can be approximated by a single-degree-of-freedom mass-spring oscillator. Hereinafter, they are referred to as parasitic beams. They were symmetrically placed at both sides of the host beam to avoid torsional motion of the host beam. The six pairs of parasitic beams from the clamping end to the free end are numbered successively as 1<sup>st</sup> resonator to 6<sup>th</sup> resonator. One-dimensional 2-node spring elements (COMBIN14) with stiffness of 6912 N/m were used to connect local resonators alternately. It is noted that the coupling spring stiffness here is half of that in the analytical model in section 2.2 ( $k_c = 13824$  N/m), because each resonator in the analytical model is equivalent to a pair of cantilever beams. The two vertical DOFs of the spring were coupled with the vertical DOFs of the centers of the left- and right-hand-side parasitic beam tip masses, respectively. The piezoelectric element was bonded onto the parasitic beam. Three-dimensional (3D) 20-node structural solid element SOLID186 was used for the beams and tip masses and 3D 20-node coupled-field solid element SOLID226 for the piezoelectric element. An acceleration field ( $a_{cc} = -1$  m/s<sup>2</sup>) was applied to the whole system. A harmonic analysis was performed to obtain the frequency responses of the steady-state displacement and voltage. Figure



4.(b) shows the finite element implementation of the electrode connection of the piezoelectric element bonded onto the parasitic beam. The voltage degrees of freedom (DOFs) on the top and bottom surfaces were coupled to provide uniform electrical potentials for emulating the electrodes. Then, the two electrodes were connected to the resistor (modelled by using CIRC94 element).

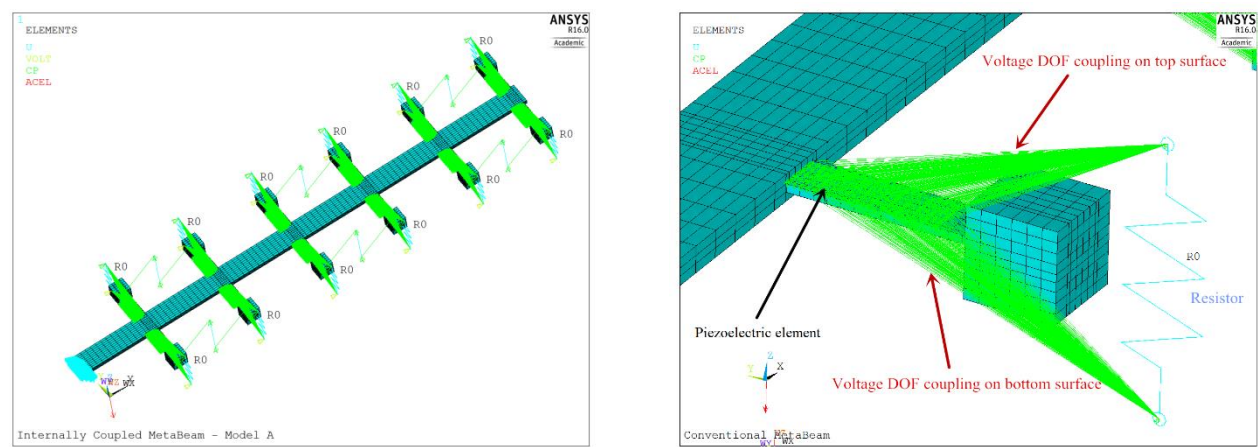


Figure 4. (a) Finite element model A of the internally coupled metamaterial beam embedded with piezoelectric elements; (b) implementation of electrode connection of piezoelectric element.

Table 2. Physical and geometric properties used in FE model.

Geometry parameters		Material parameters	
Host beam length	0.45 m	Host beam material density	7860 kg/m <sup>3</sup>
Host beam width	0.020 m	Host beam Young's Modulus	200×10 <sup>9</sup> Pa
Host beam thickness	0.004 m	Parasitic beam material density	2700 kg/m <sup>3</sup>
Parasitic beam length	0.0282 m	Parasitic beam Young's Modulus	69.5×10 <sup>9</sup> Pa
Parasitic beam width	0.0078 m	Tip mass material density	7860 kg/m <sup>3</sup>
Parasitic beam thickness	0.0012 m	Tip mass Young's Modulus	200×10 <sup>9</sup> Pa
Tip mass length	0.0136 m	Piezoelectric material density	5440 kg/m <sup>3</sup>
Tip mass width	0.0136 m	Piezoelectric material Young's Modulus	30.336×10 <sup>9</sup> Pa
Tip mass thickness	0.0136 m	Strain coefficient of piezoelectric layer	-170 pC/N
Piezoelectric layer length	0.022 m	Permittivity component at constant strain	1.3281×10 <sup>-8</sup> F/m
Piezoelectric layer width	0.0062 m	Global damping ratio	0.009
Piezoelectric layer thickness	0.0002 m		

### Vibration suppression of model A

Figure 5.(a) shows the transmittance predicted by model A. Geometry and material parameters used in the analysis are listed in Table 2. By removing the internal coupling springs, a conventional metamaterial beam PEH presented in [23] is obtained and the result is also provided in Figure 5.(a) for comparison. It can be observed that the first band gap (87.4-121.6 Hz) of model A is almost the same as that of the conventional one. An additional bang gap (152.6-158.3 Hz) appears although it is relatively narrow compared with the first one. Figure 5.(b) compares the results from model A and the analytical model. It is noted that their predictions of band gaps are qualitatively in a good agreement. However, though the parameters of the parasitic beam and the coupling spring are carefully selected to make model A behave as closely as possible to the analytical model with lumped resonators, the results are not completely consistent. It is noted that the analytical transmittance curve matches well with the FEA one before 100 Hz but deviates after 100 Hz. It has been checked that in the analytical calculation, sufficient modes have been used to guarantee the convergence. This deviation comes from the increasing difference between the behavior of the lumped model and the cantilever with tip mass model for the local resonator when the frequency increases beyond 100 Hz.

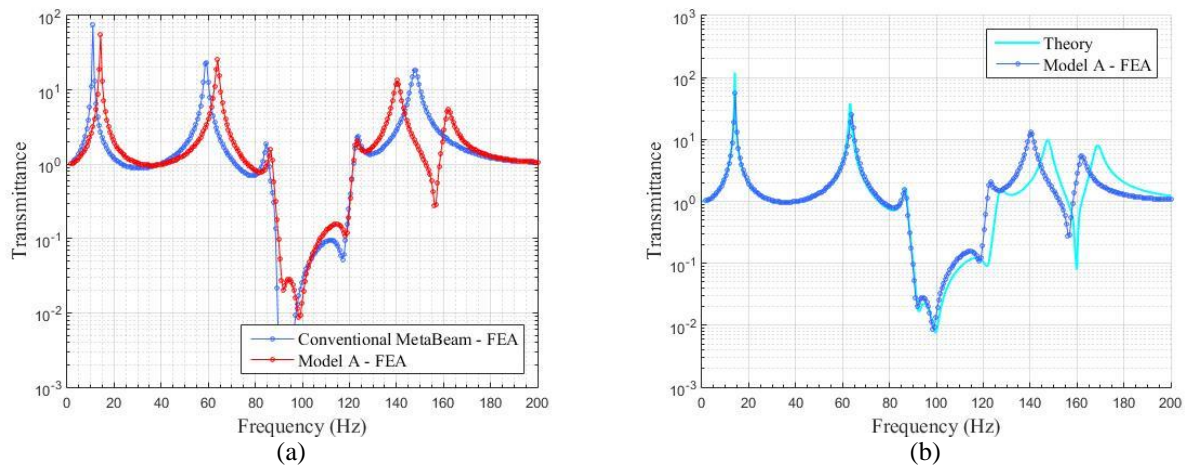


Figure 5. (a) Comparison of transmittances between the internally coupled metamaterial beam (model A) and the conventional metamaterial beam from finite element analysis; (b) comparison between FE model A and analytical result.

To further explore the phenomenon of the second band gap in the internally coupled metamaterial beam, Figure 6 shows the steady-state vibration amplitude contours of the conventional metamaterial beam and the modified metamaterial beam (model A) at 156.22 Hz (which is within the second band gap of model A). As compared to the conventional metamaterial beam, the vibration of model A is suppressed significantly. The vibration energy of the host beam decays along the beam. It is noteworthy that the resonant frequency of the parasitic beam is around 90 Hz, and the vibration suppression occurs at 156.22 Hz is due to the existence of the second band gap brought by internal couplings.

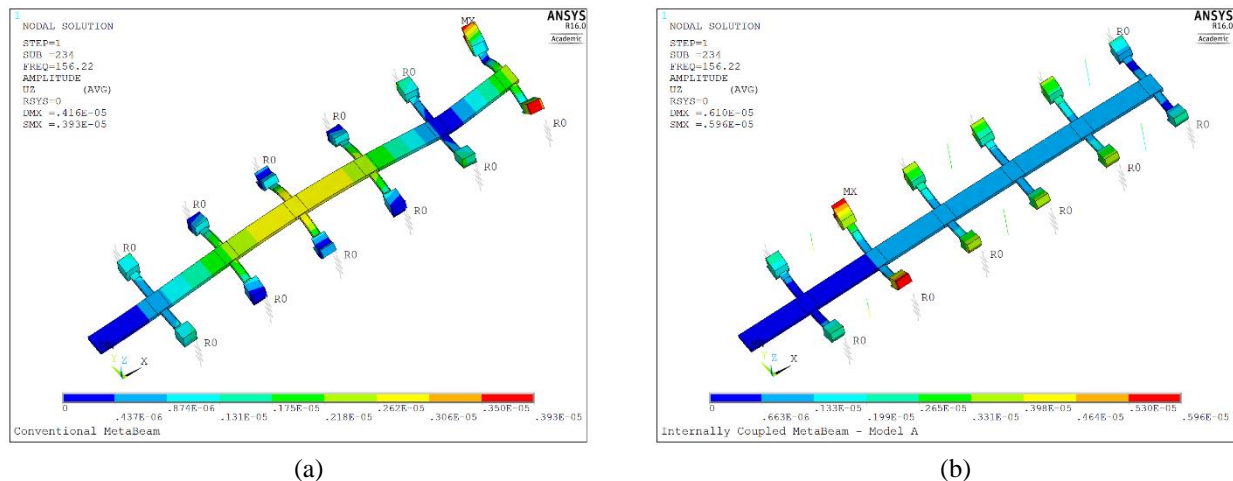


Figure 6. Steady-state vibration amplitude contours of (a) the conventional metamaterial beam, and (b) the internally coupled metamaterial beam – model A at 156.22 Hz.

### Energy harvesting of model A

By removing the internal coupling springs, the energy harvesting performance of the conventional metamaterial PEH is first investigated for later comparison with that of the modified one. Figure 7.(a) shows the open circuit voltage responses of the piezoelectric elements bonded onto those 6 parasitic beams over 0-200 Hz. It is noted that the first peak has the largest amplitude (with a low frequency resolution). With a higher frequency resolution, Figure 7.(b) shows the open circuit voltage responses around the first peak. It can be found that the maximum open circuit voltage amplitude is 20.54 V at 11 Hz. Figure 7.(c) shows the steady-state open circuit voltage contour at 11 Hz. The contour plot shows that the piezoelectric element embedded with the parasitic beam at the utmost tip of the host beam produces the largest open-circuit voltage. Moreover, the closer the parasitic beam is to the clamping end of the host beam, the lower the produced voltage is. The voltage produced by the piezoelectric parasitic beam near the clamping end of the host beam is too small for practical use.

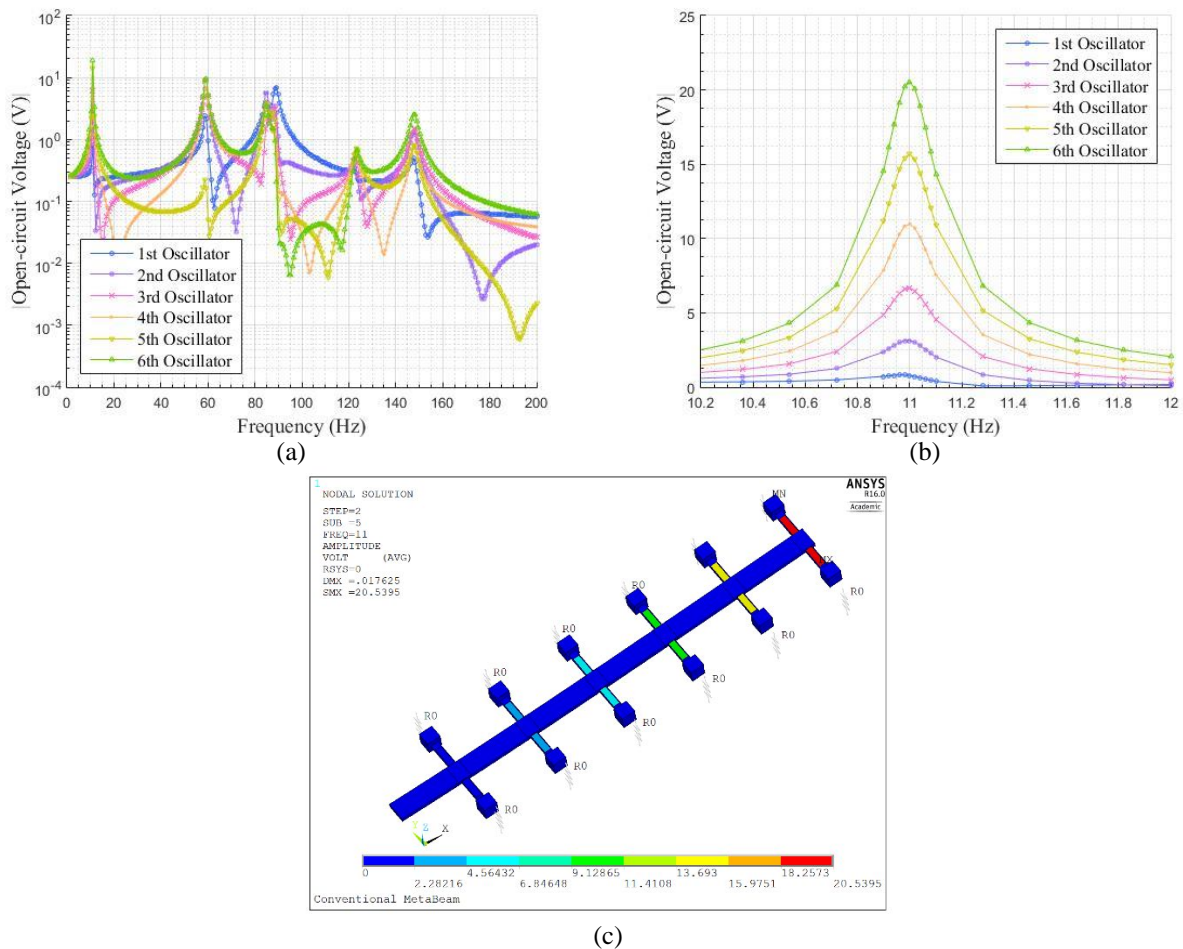


Figure 7. Open circuit voltage responses of the piezoelectric elements embedded in the conventional metamaterial beam: (a) over spectrum of 0-200Hz; (b) around first resonance with a higher resolution; and (c) open circuit voltage contour at 11 Hz.

For model A, the open circuit voltage responses of the piezoelectric elements bonded onto those 6 pairs of parasitic beams are shown in Figure 8.(a). It is noted that these piezoelectric elements provide the largest open circuit voltages around the first resonant frequency than higher resonant frequencies. Similarly, with a high frequency resolution, Figure 8.(b) shows the responses around the first peak with higher resolution. It can be found that the maximum voltage amplitude of 80.08 V is achieved at a frequency of 14.12 Hz (see Figure 8.(b)) which represents a 290% increase as compared to that of the conventional metamaterial beam PEH (Figure 7.(b)). This indicates that the energy harvesting performance of model A is much improved due to the existence of the internal coupling.

The steady-state open circuit voltage contour at 14.12 Hz is demonstrated in Figure 8.(c). It is noted that the electric potential distribution is different from that of the conventional metamaterial beam PEH. Due to the existence of the internal coupling, the 5<sup>th</sup> rather than the 6<sup>th</sup> parasitic beam associated piezoelectric element is the most efficient one. Overall, all the piezoelectric elements' voltage outputs (Figure 8.(b)) have been significantly enhanced as compared to those of the conventional metamaterial beam PEH (Figure 7.(b)). Therefore, from the perspective of energy harvesting, the introduction of the internal coupling is favorable. This is also consistent with what was concluded in the analytical study.

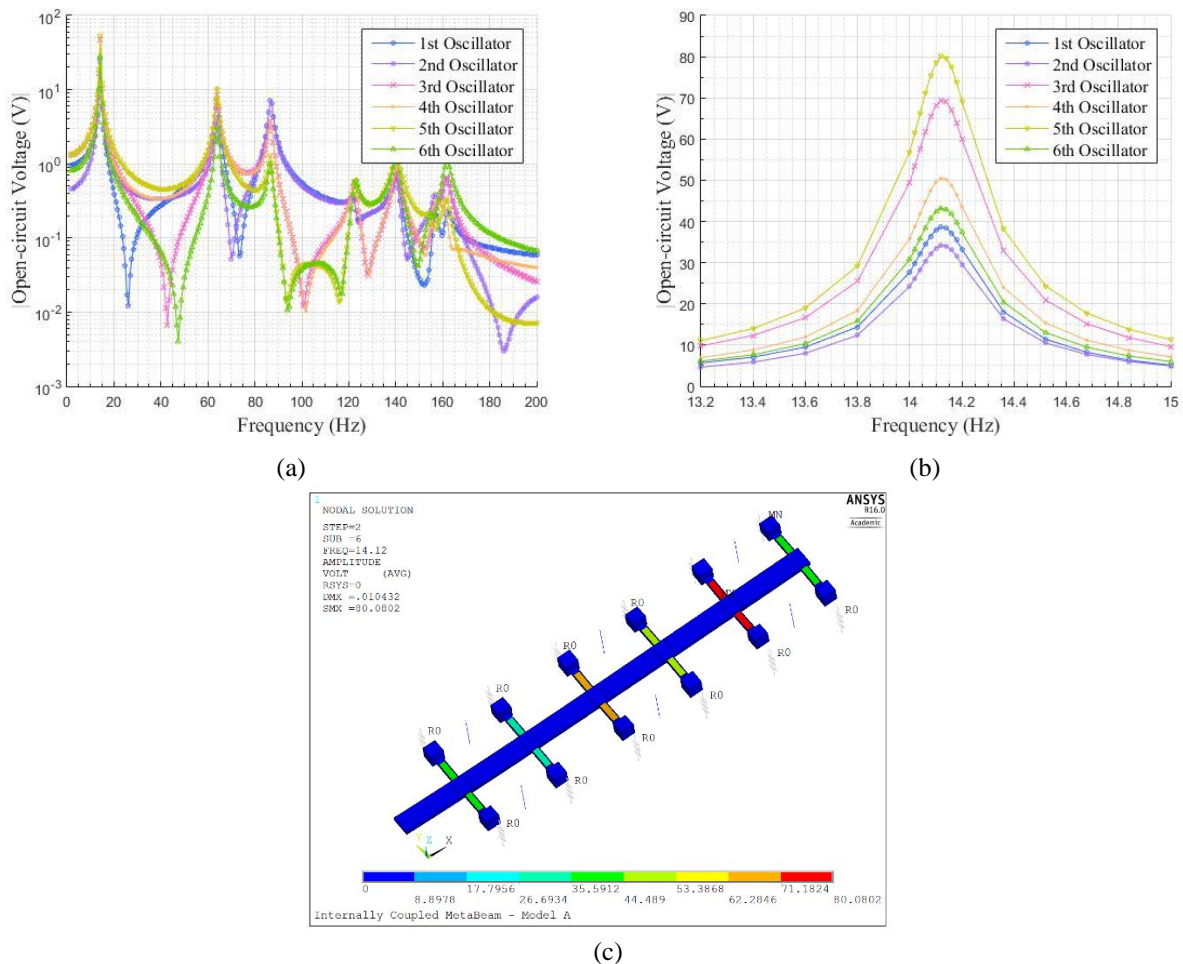


Figure 8. Open circuit voltage responses of the piezoelectric elements embedded in the internally coupled metamaterial beam – model A: (a) over spectrum of 0-200 Hz, (b) around first resonance with a higher resolution, and (c) open circuit voltage contour at 14.12 Hz.

### 3.2 Modified piezoelectric metamaterial beam - model B

Considering that model A is not easy to achieve (the implementation of the spring connection), an alternative finite element model (model B) is established as shown in Figure 9. In this model, the internal coupling spring is replaced by a thin beam, which connects the tip masses of the left- and right-hand-side parasitic beams. The material properties of the connection beam are the same as those of the host beam. The geometry parameters are as follows: width is 0.008 m, thickness is 0.001 m and length is 0.0614 m (determined by other dimension parameters of the metamaterial beam). The connection beam is roughly considered as a guided beam [27] whose effective stiffness of is 6912 N/m after theoretical calculation. It is noteworthy that these parameters are carefully selected to make the beam connection roughly comparable with the spring connection in model A. The same excitation and boundary conditions as for model A are applied to model B.



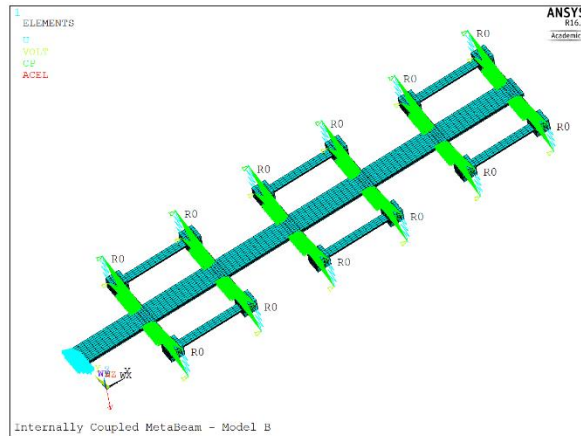


Figure 9. Finite element model B of the internally coupled metamaterial beam embedded with piezoelectric elements.

### ***Vibration suppression of model B***

Figure 10 shows the transmittance of model B. The width of the first band gap (83.3-115.8 Hz) still has a minor difference as compared to the conventional metamaterial beam (85.9-121.7 Hz), but the band gap moves towards low frequency slightly. Like model A, there also appears a second band gap (125.6-156.2 Hz). However, the behavior of the second band gap is quite different from that of both model A and the analytical model (Figure 5.(b)). The width of the second band gap is much larger than the analytical prediction and becomes comparable to the width of the first band gap.

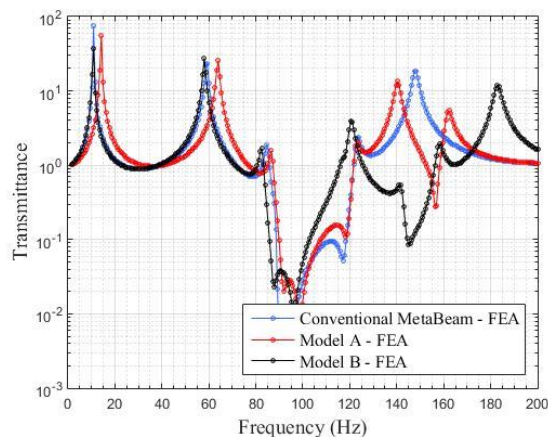


Figure 10. Comparison of transmittances of the internally coupled metamaterial beam (model A & model B) and the conventional metamaterial beam from finite element analysis.

To further investigate the vibration behavior of the system in the second band gap, Figure 11 presents the steady-state vibration amplitude contours of the conventional metamaterial beam (FE model), model A and model B at 142.29 Hz (within the second band gap of model B). It is noted that the vibration of model B is significantly suppressed. The vibration energy decays rapidly along the length of the host beam.

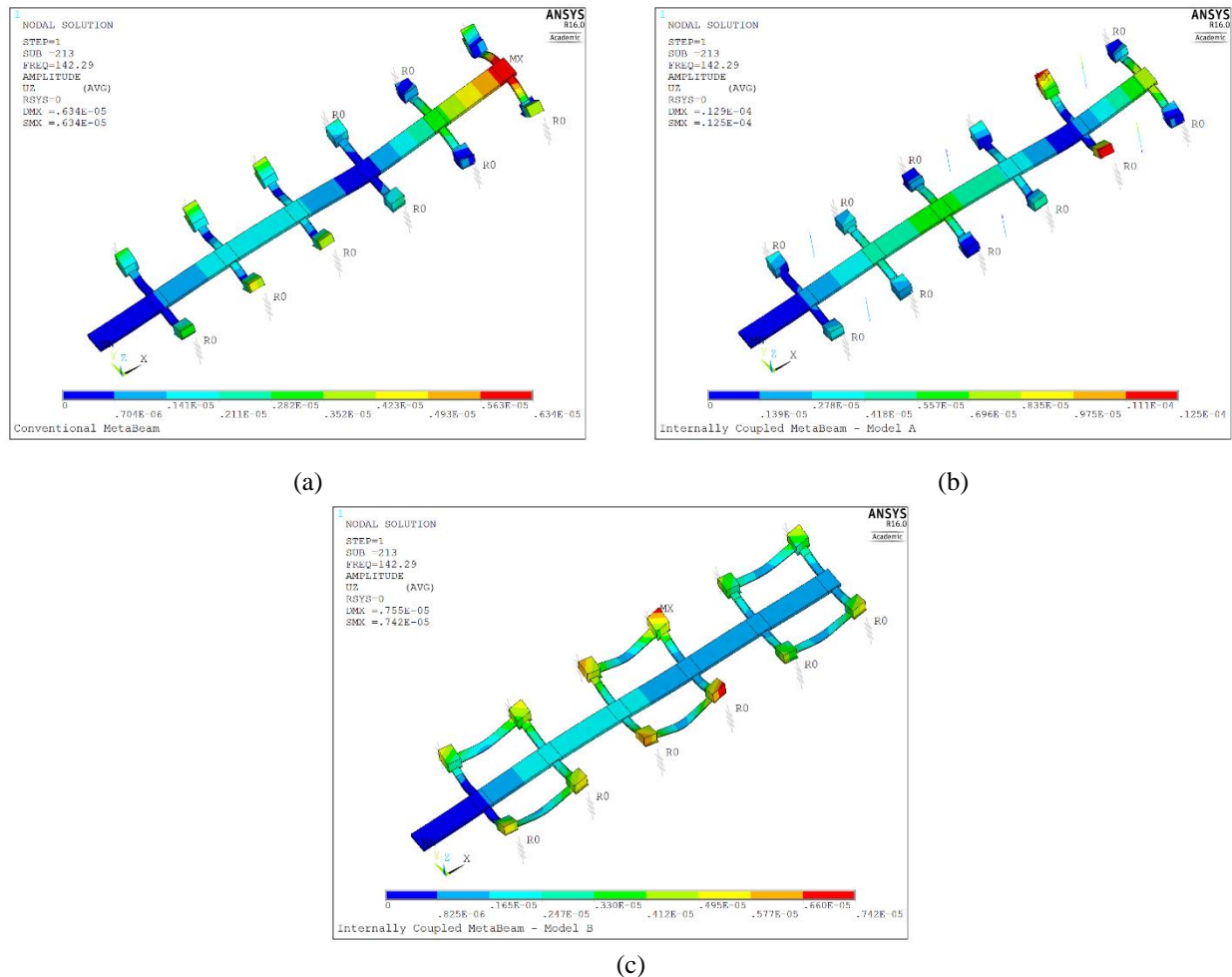


Figure 11. Steady-state vibration amplitude contours of (a) the conventional metamaterial beam, (b) the internally coupled metamaterial beam – model A, and (c) internally coupled metamaterial beam – model B at 142.29 Hz.

### Energy harvesting of model B

The open circuit voltage frequency responses of the piezoelectric elements bonded onto the 6 pairs of parasitic beams of model B are shown in Figure 12.(a). Around the first resonant frequency, these piezoelectric elements provide the largest open-circuit voltages, as anticipated. Figure 12.(b) shows the responses around the first peak with a higher frequency resolution. The corresponding steady-state open circuit voltage contour plot is shown in Figure 12.(c).

In contrast to model A, the enhancement in the voltage output is not observed in model B, and the maximum voltage amplitude of model B is even slightly decreased to 20.50 V as compared to that of the conventional one (Figure 7.(b)). Although the voltage output of the 6<sup>th</sup> piezoelectric element remains almost unchanged, the voltage output of the 5<sup>th</sup> one is enhanced from 15.68 to 19.05 V, providing a similar energy harvesting ability as that of 6<sup>th</sup> element (Figure 12.(b)). This is because near the first resonant frequency, motions of all parasitic beams are almost in phase (but not completely because of damping). The introduction of connection beams forced the neighbouring two coupled parasitic beams to behave almost the same. Overall, the energy harvesting performance of model B is slightly improved as compared to that of the conventional metamaterial beam PEH.

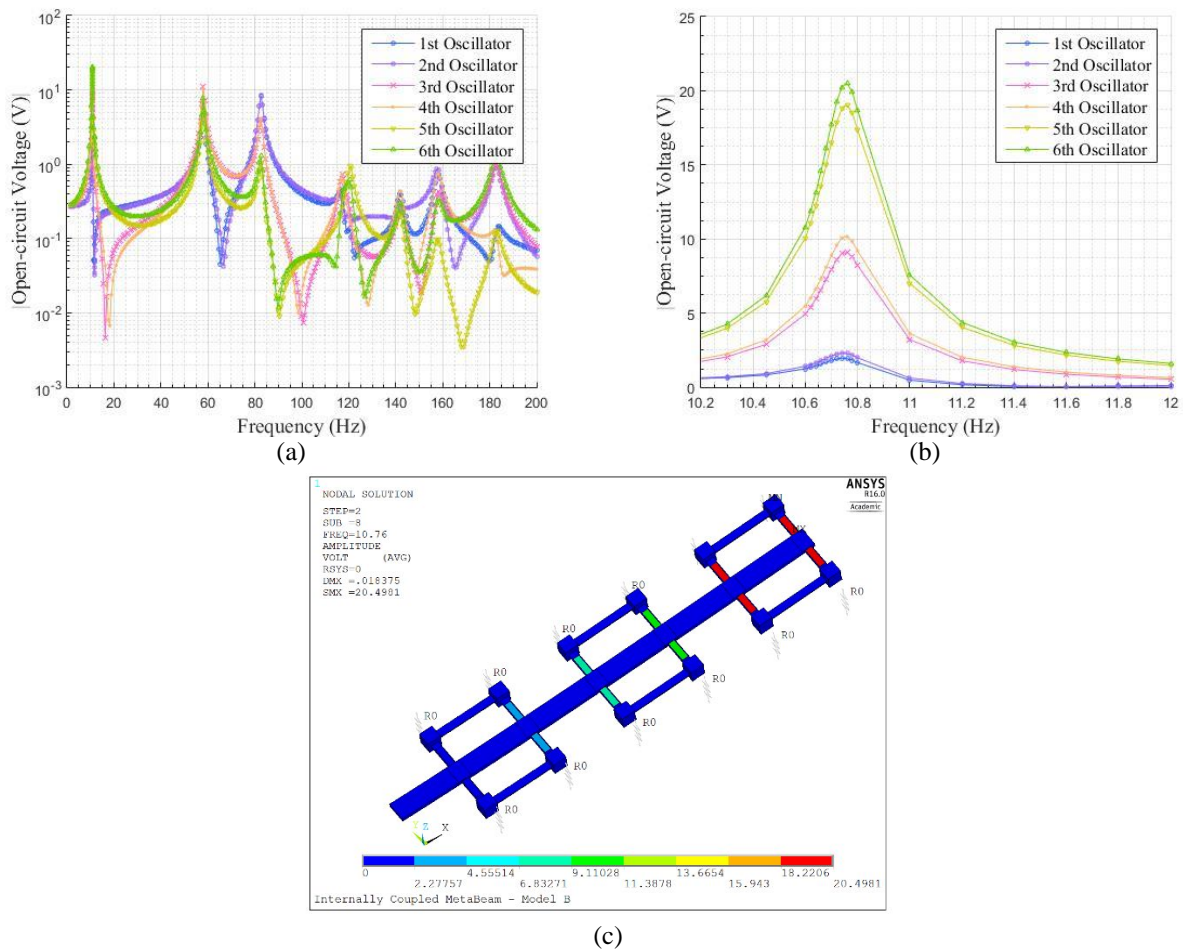


Figure 12. Open circuit voltage responses of the piezoelectric elements embedded in the internally coupled metamaterial beam – model B: (a) over spectrum of 0-200Hz, (b) around first resonance with a higher resolution, and (c) open circuit voltage contour at 10.76 Hz.

### A supplementary parametric study

As model B has a different dynamic behavior from the analytical model and model A (which is proved to be equivalent to the analytical model), the investigation of the effect of the connection beam thickness on model B's performances is supplemented. Figure 13 shows the transmittances of model B with various connection beam thicknesses. The increase in the thickness of the connection beam actually indicates the increase of the effective stiffness of the beam connection. With the increase in the thickness of the coupling beam, it is noted that similar to the analytical model, the first band gap is almost unaffected and the location of the second band gap moves toward a higher frequency. In addition, both the depth and the width of the valley that represents the second band gap increases evidently. Therefore, to achieve an enhanced second band gap for an improved vibration suppression ability, the connection beam is suggested to be designed thicker.

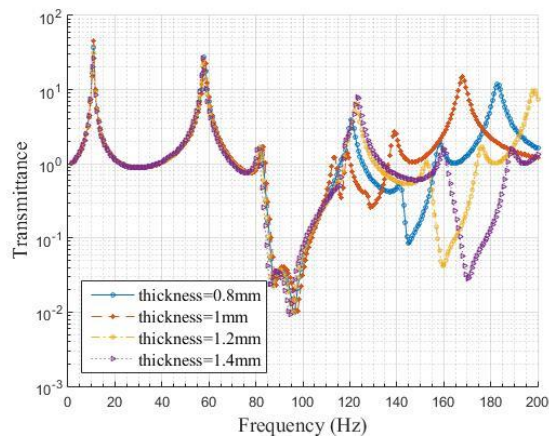


Figure 13. Transmittances of the internally coupled metamaterial beam - model B for different connection beam thicknesses.

Figure 14 shows the open circuit voltage responses of the piezoelectric elements embedded in model B for different connection beam thicknesses. It is noted that the influence of the connection beam thickness on the open circuit voltage responses is minor (the maximum amplitude is nearly unchanged). With the increase in the connection beam thickness, only the peak location slightly moves toward lower frequency. This is because the overall mass of the system is slightly increased and the eigen-frequencies of the system decrease.

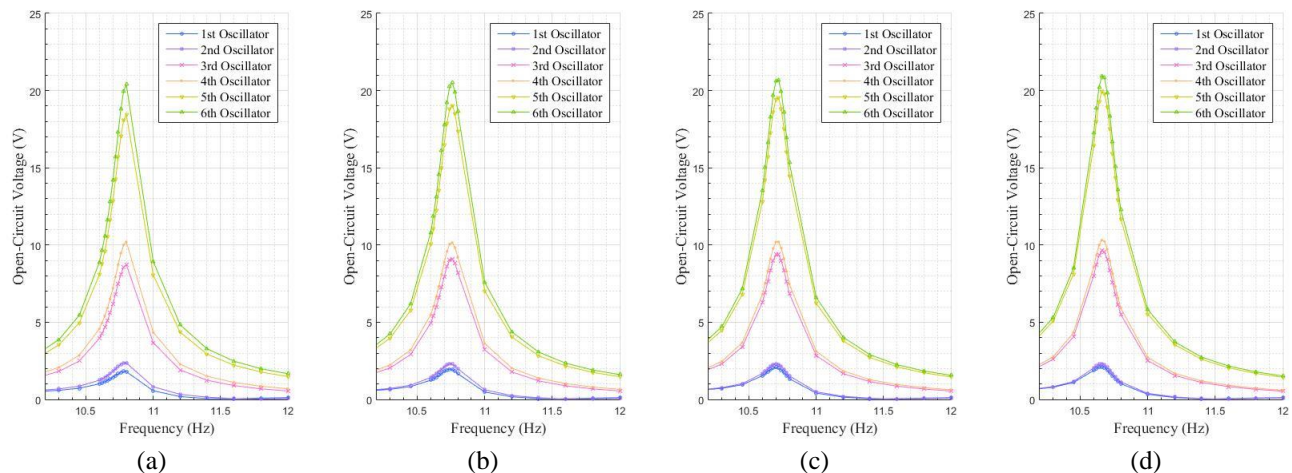


Figure 14. Open circuit voltage responses of the embedded piezoelectric elements in the internally coupled metamaterial beam – model B for different connection beam thicknesses: (a) 0.8mm; (b) 1mm; (c) 1.2mm; (d) 1.4mm.

### 3.3 Discussion of the difference between model A and model B

The reason of the difference between model A and model B is of our interest. First, it is wondered whether the mass of the beam connection has a significant influence on this system and thus resulting in a quite different dynamic behavior of model B. Second, the effective coupling stiffness of the beam connection is carefully checked through finite element simulations, rather than by roughly considering it as a guided beam.

In the following, at first, the mass of the connection beam is reduced to be negligible to see its effect on the dynamic behavior of the whole system. Figure 15 shows the transmittances of the case with connection beams of normal mass density  $7860 \text{ kg/m}^3$  and with a quasi-zero mass density  $1 \text{ kg/m}^3$ . It can be seen that even the mass of the connection beam is quasi-zero, there is no significant influence on the transmittance and the only change is that all the modes slightly move toward a higher frequency. This is because the overall mass of the system is reduced. Figure 16(a) and (b) show the open circuit voltage responses of the two cases. It can be noted that again no evident change occurs in the open circuit voltage response, except that the peak slightly moves toward a high frequency with a minor decrease in the magnitude.



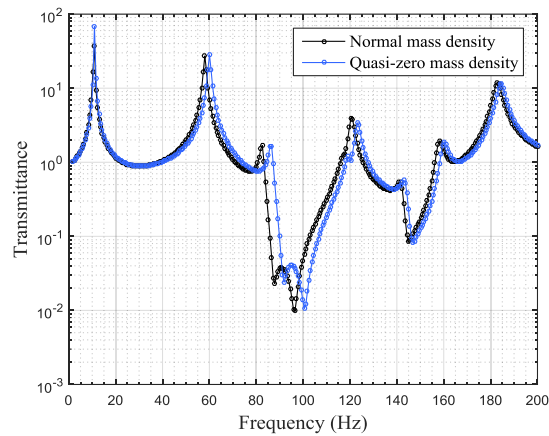


Figure 15. Comparison of the transmittances of the internally coupled metamaterial beam - model B with coupling beams of normal mass density and of quasi-zero mass density.

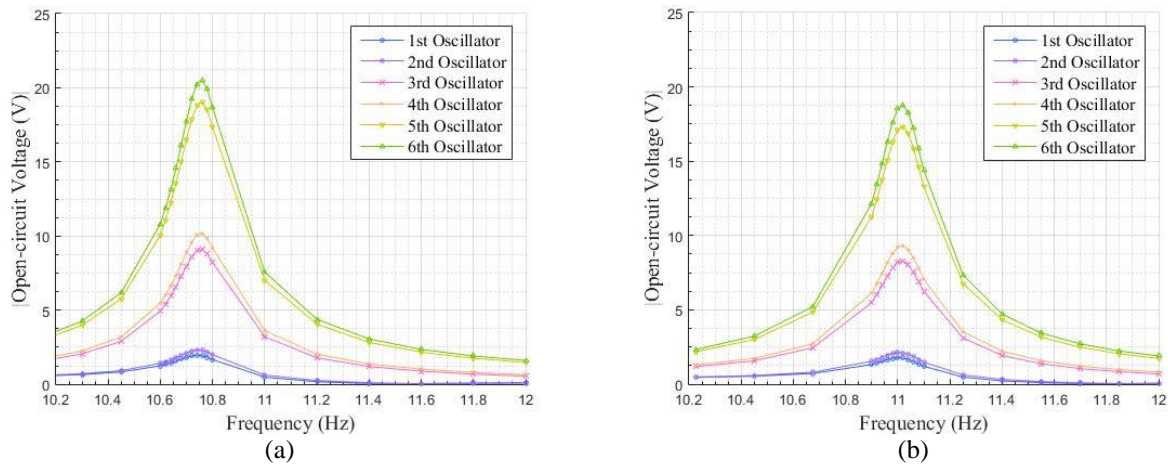


Figure 16. Open-circuit voltage responses of the piezoelectric elements embedded in the internally coupled metamaterial beam – model B: (a) with coupling beams of normal mass density; (b) with coupling beams of quasi-zero mass density.

Later, the effective stiffness of the beam connection is carefully checked and compared with that of the spring connection. Consider one pair of coupled neighbouring parasitic beams with their roots clamped. A displacement load ( $U_{Z1} = 10 \text{ mm}$ ) is applied on the left-hand-side tip mass. A static analysis is then performed.

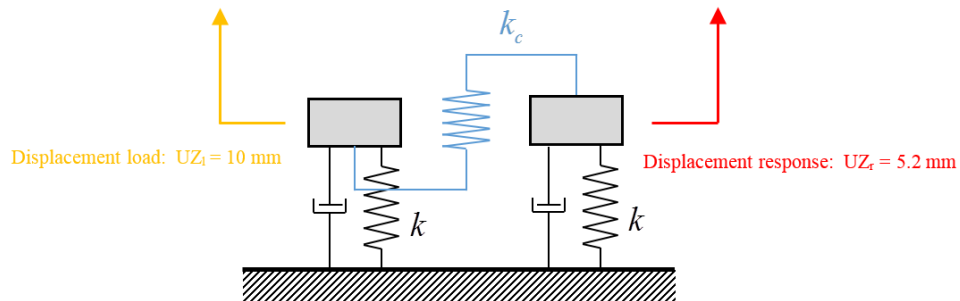


Figure 17. Equivalent lumped model under investigation.

At first, a simple theoretical analysis is conducted with a lumped parameter model shown in Figure 17. With the displacement load ( $UZ_l = 10$  mm) applied on the left hand side oscillator, the displacement response of the right-hand-side oscillator can be calculated:

$$UZ_r = 10 \frac{k_c}{k + k_c} = 5.2 \text{ mm} \quad (14)$$

The following presents the finite element static analysis results. For the case of spring connection as shown in Figure 18.(a), the displacement response of the central point on the top surface of the right-hand-side tip mass in the Z-axis direction is 5.076 mm. While, under the same boundary conditions and the same displacement load, for the case of beam connection as shown in Figure 18.(b), the corresponding displacement response is 1.992 mm. Hence, it can be seen that the beam connection is inherently different from the spring connection, though both types of connections are intended to provide the force coupling between the neighbouring two parasitic beams (i.e., local resonators). Therefore, it is not surprising that the performances of model A and model B are different.

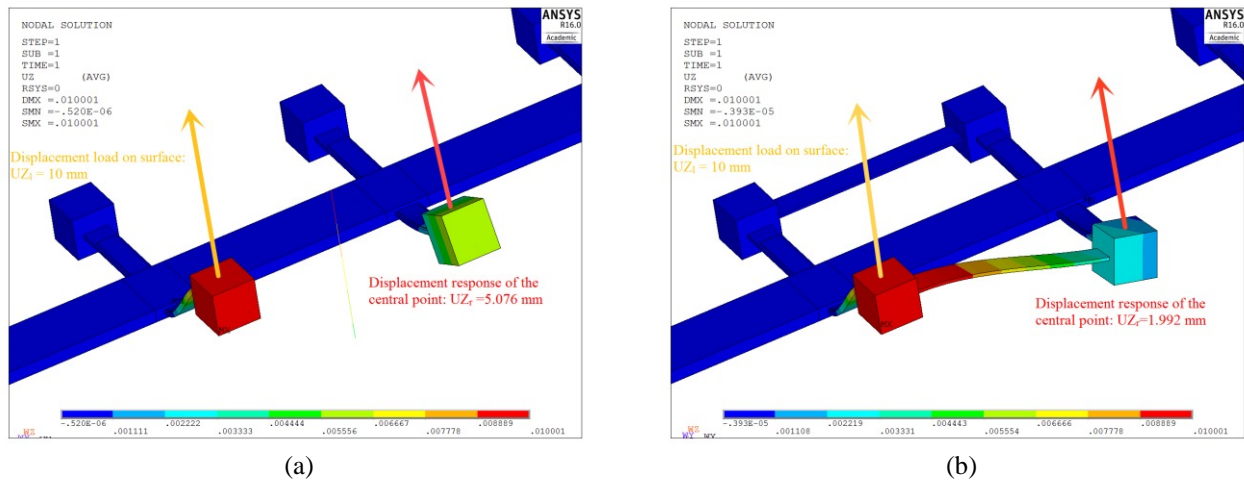


Figure 18. Contours of displacement responses of: (a) model A; (b) model B under a static force load.

#### 4. CONCLUSIONS

This paper has proposed and investigated an internally coupled metamaterial beam embedded with piezoelectric elements for both vibration suppression and energy harvesting. The transmittance of a finitely long model is derived. This demonstrated the occurrence of an additional band gap due to the existence of the internal coupling. The theoretical study also shows that not only the vibration suppression ability can be slightly enhanced, but also the energy harvesting performance can be significantly improved by using the modified metamaterial beam, as compared to the conventional one without internal coupling. In addition to the analytical model, a finite element model (model A), which is equivalent to the analytical model in respect of the internal coupling, is developed. The FE results are in good agreement with those of the analytical model and confirm both the vibration suppression and energy harvesting performance improvement of the proposed internally coupled metamaterial beam PEH. Another finite element model (model B), which represents a more practical implementation, is also established in which the internal coupling is realized by a thin beam connection rather than an ideal spring connection. It is found that although the internal coupling using such a beam connection does not provide much improvement in energy harvesting as compared to the conventional metamaterial beam PEH, the vibration suppression ability is greatly improved with a much wider second band gap than that obtained from model A. The difference between the performances of model A and B, originating from the inequivalence of the beam connection and coupling spring is then discussed. The analytical model and the finite element models developed in the work provide useful tools to design internally coupled piezoelectric metamaterial beams for concurrent efficient energy harvesting and vibration suppression.

## REFERENCES

- [1] Shalaev, V.M., Cai, W., Chettiar, U.K., Yuan, H.K., Sarychev, A.K., Drachev, V.P., and Kildishev, A.V., "Negative index of refraction in optical metamaterials," *Optics Letters* 30(24), 3356-3358 (2005).
- [2] Yao, J., Liu, Z., Liu, Y., Wang, Y., Sun, C., Bartal, G., Stacy, A.M., and Zhang, X., "Optical negative refraction in bulk metamaterials of nanowires," *Science* 321(5891), 930 (2008).
- [3] Huang, H. and Sun, C., "Anomalous wave propagation in a one-dimensional acoustic metamaterial having simultaneously negative mass density and Young's modulus," *Journal of The Acoustical Society of America* 132(4), 2887-2895 (2012).
- [4] Liu, X., Hu, G., Huang, G., and Sun, C., "An elastic metamaterial with simultaneously negative mass density and bulk modulus," *Applied Physics Letters* 98(25), 251907 (2011).
- [5] Yao, S., Zhou, X., and Hu, G., "Experimental study on negative effective mass in a 1D mass-spring system," *New Journal of Physics* 10(4), 043020 (2008).
- [6] Huang, H., Sun, C., and Huang, G., "On the negative effective mass density in acoustic metamaterials," *International Journal of Engineering Science* 47(4), 610-617 (2009).
- [7] Xu, J. and Tang, J., "Tunable prism based on piezoelectric metamaterial for acoustic beam steering," *Applied Physics Letters* 110(18), 181902 (2017).
- [8] Ho, K.M., Yang, Z., Zhang, X., and Sheng, P., "Measurements of sound transmission through panels of locally resonant materials between impedance tubes," *Applied Acoustics* 66(7), 751-765 (2005).
- [9] Oudich, M., Assouar, M.B., and Hou, Z., "Propagation of acoustic waves and waveguiding in a two-dimensional locally resonant phononic crystal plate," *Applied Physics Letters* 97(19), 193503 (2010).
- [10] Shen, L., Wu, J., Zhang, S., Liu, Z., and Li, J., "Low-frequency vibration energy harvesting using a locally resonant phononic crystal plate with spiral beams," *Modern Physics Letters B* 29(1), 1450259 (2015).
- [11] Zhou, X. and Hu, G., "Superlensing effect of an anisotropic metamaterial slab with near-zero dynamic mass," *Applied Physics Letters* 98(26), 263510 (2011).
- [12] Zhu, R., Liu, X., Hu, G., Sun, C., and Huang, G., "A chiral elastic metamaterial beam for broadband vibration suppression," *Journal of Sound and Vibration* 333(10), 2759-2773 (2014).
- [13] Liu, Y., Yu, D., Li, L., Zhao, H., Wen, J., and Wen, X., "Design guidelines for flexural wave attenuation of slender beams with local resonators," *Physics Letters A* 362(5), 344-347 (2007).
- [14] Xiao, Y., Wen, J., Huang, L., and Wen, X., "Analysis and experimental realization of locally resonant phononic plates carrying a periodic array of beam-like resonators," *Journal of Physics D: Applied Physics* 47(4), 045307 (2013).
- [15] Gao, N., Wu, J., Hou, H., and Yu, L., "Excellent low-frequency sound absorption of radial membrane acoustic metamaterial," *International Journal of Modern Physics B* 31(3), 1750011 (2017).
- [16] Milton, G.W. and Willis, J.R. "On modifications of Newton's second law and linear continuum elastodynamics," *Proceedings of the Royal Society of London A: Mathematical, Physical and Engineering Sciences* 463(2079), 855-880 (2007).
- [17] Huang, H. and Sun, C., "Wave attenuation mechanism in an acoustic metamaterial with negative effective mass density," *New Journal of Physics* 11(1), 013003 (2009).
- [18] Erturk, A. and Inman, D.J., "A distributed parameter electromechanical model for cantilevered piezoelectric energy harvesters," *Journal of Vibration and Acoustics* 130(4), 041002 (2008).
- [19] Xu, J. and Tang, J., "Modeling and analysis of piezoelectric cantilever-pendulum system for multi-directional energy harvesting," *Journal of Intelligent Material Systems and Structures* 28(3), 323-338 (2017).
- [20] Tao, K., Tang, L., Wu, J., Lye, S.W., Chang, H., and Miao, J., "Investigation of Multimodal Electret-based MEMS Energy Harvester with Impact-induced Nonlinearity," *Journal of Microelectromechanical Systems*, (2018).
- [21] Mikoshiba, K., Manimala, J.M., and Sun, C., "Energy harvesting using an array of multifunctional resonators," *Journal of Intelligent Material Systems and Structures* 24(2), 168-179 (2013).
- [22] Hu, G., Tang, L., Banerjee, A., and Das, R., "Metastructure With Piezoelectric Element for Simultaneous Vibration Suppression and Energy Harvesting," *Journal of Vibration and Acoustics* 139(1), 011012 (2017).
- [23] Hu, G., Tang, L., and Das, R. "Metamaterial-inspired piezoelectric system with dual functionalities: energy harvesting and vibration suppression," *SPIE Smart Structures and Materials+ Nondestructive Evaluation and Health Monitoring* 10164, 10 (2017).

- [24]Chen, Z., Guo, B., Yang, Y., and Cheng, C., "Metamaterials-based enhanced energy harvesting: A review," *Physica B-Condensed Matter* 438, 1-8 (2014).
- [25]Hu, G., Tang, L., Das, R., Gao, S., and Liu, H., "Acoustic metamaterials with coupled local resonators for broadband vibration suppression," *AIP Advances* 7(2), 025211 (2017).
- [26]Aldraihem, O. and Baz, A., "Energy harvester with a dynamic magnifier," *Journal of Intelligent Material Systems and Structures* 22(6), 521-530 (2011).
- [27]Gere, J.M. and Goodno, B.J., "Mechanics of materials," Cengage Learning, (2011).